

Intramolecular vibrations complement the robustness of primary charge separation in the Photosystem II reaction center

Yuta Fujihashi,¹ Masahiro Higashi,² and Akihito Ishizaki^{1,3,*}

¹*Institute for Molecular Science, National Institutes of Natural Sciences, Okazaki 444-8585, Japan*

²*Department of Chemistry, Biology, and Marine Science,
University of the Ryukyus, 1 Senbaru, Nishihara, Okinawa 903-0213, Japan*

³*School of Physical Sciences, The Graduate University for Advanced Studies, Okazaki 444-8585, Japan*

(Dated: December 14, 2024)

The energy conversion of oxygenic photosynthesis is triggered by primary charge separation in proteins at the photosystem II reaction center. Here, we investigate the impacts of the protein environment and intramolecular vibrations on primary charge separation at the photosystem II reaction center. This is accomplished by combining the quantum dynamic theories of condensed phase electron transfer with quantum chemical calculations to evaluate the vibrational Huang-Rhys factors of chlorophyll and pheophytin molecules. We report that individual vibrational modes play a minor role in promoting the charge separation, contrary to the discussion in recent publications. Nevertheless, these small contributions accumulate to considerably influence the charge separation rate, resulting in sub-picosecond charge separation almost independent of the driving force and temperature. We suggest that the intramolecular vibrations complement the robustness of the charge separation in the photosystem II reaction center against the inherently large static disorder of the involved electronic energies.

I. INTRODUCTION

Energy conversion in photosynthesis starts with the absorption of a sunlight photon by one of the light-harvesting pigments, followed by the transfer of electronic excitation energy to the protein at the reaction center (RC), where charge separation is initiated. In particular, oxygenic photosynthesis in plants, cyanobacteria, and algae begins in photosystem II (PSII)^{1,2} (Fig. 1). The PSII RC contains six chlorophyll (Chl) and two pheophytin (Pheo) molecules arranged in the form of two nearly symmetric branches corresponding to the D1 and D2 proteins. The PSII RC and the well-investigated purple bacterial RC share considerable similarity in the arrangement of their redox cofactors,³ and thus it was speculated that the manner of primary charge separation in the PSII RC would be similar to that of purple bacteria. In the mid-1990s, however, it was recognized that the charge separation in the PSII RC most likely proceeded in a manner that is different from that at the purple bacterial RC.⁴⁻⁷ In the 2000s, the nature of the primary charge separation in the PSII RC was investigated by independent studies with the use of femtosecond pump-probe spectroscopy in the visible/mid-infrared⁸ and visible⁹ spectral regions. Both reports identified the accessory chlorophyll (Chl_{D1}) as the primary electron-donor and pheophytin (Pheo_{D1}) as the primary electron-acceptor. Time constants of 600–800 fs⁸ and 3 ps⁹ were extracted for the pheophytin reduction, which yield values of 200–300 fs and 1 ps as the intrinsic time constant of the primary charge separation.¹ In addition, theoretical analyses of time-dependent emission from the PSII core complex yielded 100 fs as the intrinsic time constant.¹⁰ Regardless of the controversial differences, all values for the PSII RC are faster than the time constant of 3 ps measured for the primary ET starting from the special pair in purple bacterial RCs.¹¹ As the coupling strengths between electron-donors and acceptors are usually thought to be of the order of tens of wavenumbers,¹¹⁻¹³ the precise mechanisms that enable sub-picosecond charge separation are to a large extent unknown.

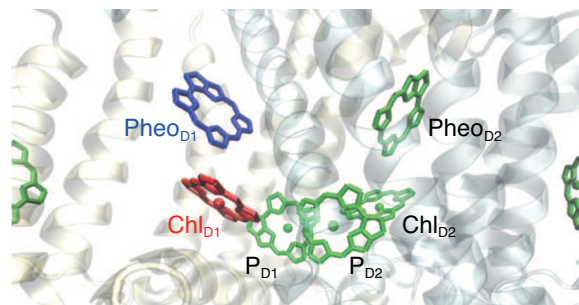


FIG. 1. The structural arrangement of pigments in the PSII reaction center. Data taken from the 4UB6 PDB structure.¹⁴ The tails of chlorophylls and pheophytins are removed for the sake of clarity.

Recently, Romero *et al.*^{7,15} and Fuller *et al.*¹⁶ revealed the presence of long-lived quantum beats in the PSII RC by means of two-dimensional (2D) electronic spectroscopy.^{17,18} Many of the observed beats possess frequencies of vibrational modes identified in resonance Raman¹⁹ and fluorescence line-narrowing spectra,²⁰ and some of the frequencies were deemed to match the frequency differences between electronic excitons and the primary charge transfer state. On the basis of the experimental observations, the authors suggested that the electronic-vibrational resonance might represent an important design principle for enabling charge separation with high quantum efficiency in oxygenic photosynthesis. Namely, resonance between an electronic exciton state and the vibrational levels in the charge-transfer state ($\text{Chl}_{D1}^+ \text{Pheo}_{D1}^-$) leads to quantum mechanically mixed electronic and vibrational states, and thereby optimizes the flow of electrons to the final charge-separated state. However, the reorganization energies and thus the protein-induced fluctuations associated with charge transfer states are generally large,²¹⁻²⁴ and hence it is questionable whether such electronic-vibrational mixtures could be robust and could play a role under the influence of the fluctuations at physiological temperatures.²⁵ Indeed, by em-

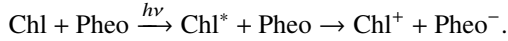
ploying numerically accurate quantum dynamics calculations, Fujihashi *et al.*²⁶ and Monahan *et al.*²⁷ demonstrated that such electronic-vibrational mixtures could not necessarily play a role in hastening electronic energy transfer in protein environments, despite contributing to the enhancement of long-lived quantum beating in 2D electronic spectra at cryogenic temperatures. Furthermore, it should be noted that the static disorder in systems with larger reorganization energy is stronger. Indeed, Gelzinis *et al.*²⁴ revealed strong static disorder ($\sim 550 \text{ cm}^{-1}$) by analyzing multiple optical spectra of the PSII RC. Hence, further investigations on the influence of intramolecular vibrations on primary charge separation are required.

In this study, we comprehensively investigate the impacts of the intramolecular vibrational modes on primary charge separation in the PSII RC by combining quantum dynamic theories of condensed phase electron transfer with quantum chemical calculations for evaluating the vibrational Huang-Rhys factors in Chl and Pheo molecules as well as the parameters extracted from experimental measurements.

II. THEORY

A. Hamiltonian of the charge separation

For the sake of simplicity, we do not consider exciton-charge-transfer states such as $(\text{Chl}^{\delta+}\text{Pheo}^{\delta-})^*$, where $\delta\pm$ indicates charge-transfer character.^{7,15} Instead, we consider a simpler scheme for the primary charge separation process,



This reaction involves three states: the electronic ground state $|g\rangle$, the photo-excited electron-donor state $|D\rangle$, and the electron-acceptor state $|A\rangle$. The dynamics of the charge separation is described by the Hamiltonian,

$$H = \sum_{m=g,D,A} H_m |m\rangle\langle m| + V_{DA}(|D\rangle\langle A| + |A\rangle\langle D|), \quad (1)$$

with $H_g = H_{\text{Chl}} + H_{\text{Pheo}}$, $H_D = H_{\text{Chl}^*} + H_{\text{Pheo}}$, and $H_A = H_{\text{Chl}^+} + H_{\text{Pheo}^-}$, where H_{Chl} , H_{Chl^*} , H_{Chl^+} , H_{Pheo} and H_{Pheo^-} represent the diabatic Hamiltonians to describe the intramolecular vibrational modes of the respective molecular states and the associated environmental degrees of freedom (DOFs). The interstate coupling, V_{DA} , is assumed to be independent of the accessible environmental and vibrational DOFs.

B. Huang-Rhys factors associated with the involved transitions

To evaluate the Huang-Rhys factors of the intramolecular vibrational modes for the transitions, $\text{Chl} \rightarrow \text{Chl}^*$, $\text{Chl}^* \rightarrow \text{Chl}^+$, and $\text{Pheo} \rightarrow \text{Pheo}^-$, we performed electronic structure calculations with both the Gaussian 16²⁸ and DUSHIN programs.²⁹ The fully optimized Cartesian displacements between the two adiabatic potential energy minima are projected onto the normal modes by using the DUSHIN program, and

thereby the dimensionless normal mode displacements and the corresponding Huang-Rhys factors are obtained. Technical details of the calculations are given in Methods. Figure 2 presents the Huang-Rhys factors for the Q_y transition of Chla calculated with the use of time-dependent density functional theory, CAM-B3LYP/6-31G(d)³⁰ with $\mu = 0.14$. For reference purposes, the experimentally evaluated Huang-Rhys factors are also presented. Figure 2a shows the Huang-Rhys factors obtained from the high-resolution fluorescence excitation spectrum of Chla in ether at 4.2 K.³¹ The calculated and experimental results are in reasonably good agreement, except for the low-frequency modes, $\omega_\xi < 150 \text{ cm}^{-1}$. The large discrepancy in the low-frequency region may be attributed to the harmonic approximation of the low-frequency vibrational modes in the DUSHIN program. Typically, low-frequency modes exhibit strong anharmonicity;³² however, the DUSHIN program²⁹ maps all of the modes onto harmonic normal modes. In what follows, the low-frequency modes ($\omega_\xi < 150 \text{ cm}^{-1}$) are excluded. Figures 2b and 2c show the Huang-Rhys factors evaluated by means of a hole-burning experiment on photosystem I isolated from the chloroplast of spinach at 1.6 K,³³ and the water-soluble chlorophyll-binding protein in cauliflower at 1.4 K,³⁴ respectively. The Huang-Rhys factors for the Q_y transition of Chla embedded in various photosynthetic proteins differ significantly from each other, indicating significant dependence of the Huang-Rhys factors and the vibrational distribution on local environments. Figures 2b and 2c also demonstrate that protein environments may increase the Huang-Rhys factors by several times compared with the calculated ones.

In contrast to the Q_y transition, the Huang-Rhys factors associated with the charge separation, $\text{Chl}^* + \text{Pheo} \rightarrow \text{Chl}^+ + \text{Pheo}^-$, are inaccessible in a spectroscopic fashion, and Fig. 3 presents the calculated Huang-Rhys factors for the transitions of (a) $\text{Chl}^* \rightarrow \text{Chl}^+$ and (b) $\text{Pheo} \rightarrow \text{Pheo}^-$. The main features are consistent with the frequencies of the dominant vibrational modes extracted from the beating of the 2D electronic spectra of the PSII RC (250 cm^{-1} , 340 cm^{-1} , and 730 cm^{-1}).^{15,16} However, it should be noticed that the protein environment may increase the Huang-Rhys factors, as was discussed in Fig. 2. This issue will be taken into account in discussing impacts of the intramolecular vibrational modes on the primary charge separation in the PSII RC (Fig. 5).

C. Expression of the charge separation rate

The non-equilibrium reorganization process of the environment may strongly influence the electron transfer reaction in the case of the large amount of reorganization energy associated with the photoexcitation.^{35,36} However, the environmental reorganization energy and the vibrational Huang-Rhys factors associated with the photoexcitation of chlorophyll in the visible region are small,^{31,37,38} and the interstate coupling V_{DA} is typically tens of wavenumbers.^{23,39} Hence, it may be assumed that the environmental reorganization is completed and the environmental and vibrational DOFs are equilibrated prior to the charge separation. In this situation, the rate of charge separation can be given by the second-order perturbative truncation

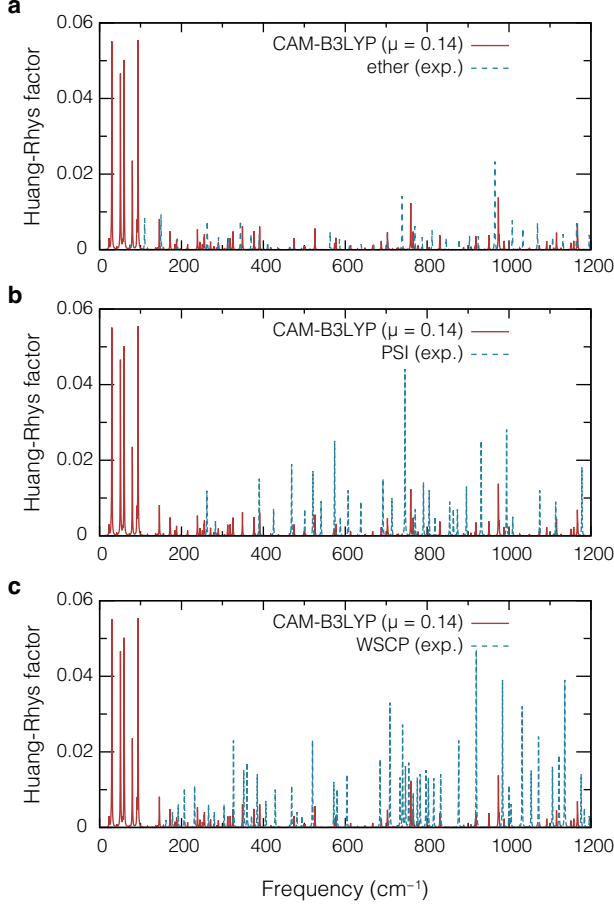


FIG. 2. Calculated Huang-Rhys factors of intramolecular vibrational modes associated with electronic excitation of chlorophyll *a*. Calculations were performed with the use of time-dependent density functional theory, CAM-B3LYP/6-31G(d)³⁰ with $\mu = 0.14$. For reference purposes, the experimentally evaluated Huang-Rhys factors are also presented: (a) high-resolution fluorescence excitation spectrum of Chla in ether at 4.2 K,³¹ (b) hole burning experiment on photosystem I at 1.6 K,^{31,33} (c) hole burning experiment on the water-soluble chlorophyll-binding protein at 1.4 K.^{31,34}

in terms of the interstate coupling V_{DA} :

$$k^{(2)} = \frac{2V_{DA}^2}{\hbar^2} \text{Re} \int_0^\infty dt \langle e^{iH_D t/\hbar} e^{-iH_A t/\hbar} \rangle_D. \quad (2)$$

In the equation, $\langle \dots \rangle_m$ denotes the statistical average with respect to the equilibrium states of the environmental and vibrational DOFs associated with the state $|m\rangle$, $\rho_m^{\text{eq}} = e^{-\beta H_m} / \text{Tr} e^{-\beta H_m}$, where β represents the inverse temperature $\beta = 1/k_B T$ with the Boltzmann constant k_B and temperature T . Here, we introduce the Franck-Condon vertical transition energy from the equilibrated electron donor state to the acceptor state, $\hbar\Omega_{AD} = \langle H_A - H_D \rangle_D$, and the collective energy gap coordinate,^{40,41} $X_{AD} = H_A - H_D - \hbar\Omega_{AD}$, which contains information on the fluctuations in the electronic energies of the electron donor and acceptor states and on the relevant nuclear dynamics. In this work, we assume that the environmentally induced fluctuations can be described as Gaussian processes⁴⁰

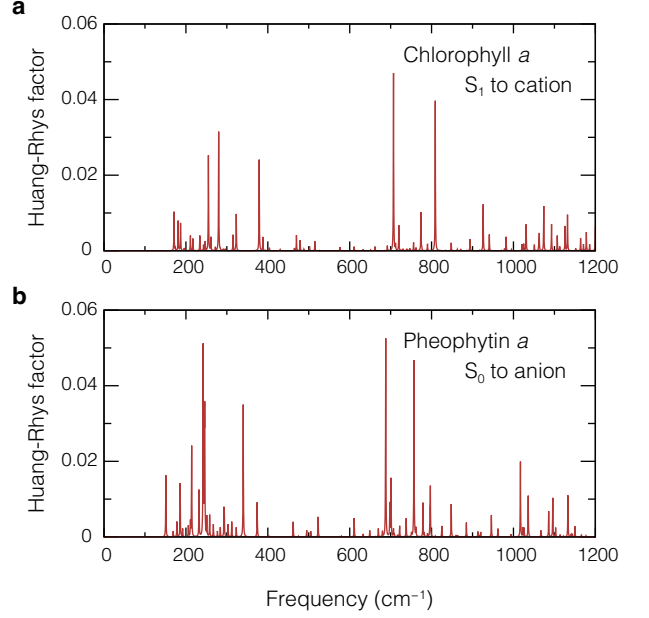


FIG. 3. Calculated Huang-Rhys factors of intramolecular vibrational modes associated with transitions involved in the charge separation. (a) $\text{Chla}^* \rightarrow \text{Chla}^+$ and (b) $\text{Pheoa} \rightarrow \text{Pheoa}^-$. The calculations were performed with the use of time-dependent density functional theory, CAM-B3LYP/6-31G(d)³⁰ with $\mu = 0.14$.

and that the relevant nuclear dynamics are harmonic. Under this assumption, Eq. (2) is recast into

$$k^{(2)} = \frac{2V_{DA}^2}{\hbar^2} \text{Re} \int_0^\infty dt \exp[-i\Omega_{AD}t - g_D(t)]. \quad (3)$$

The Franck-Condon vertical transition energy $\hbar\Omega_{AD}$ is expressed as

$$\hbar\Omega_{AD} = \Delta G^\circ + \lambda_{AD} + \hbar \sum_{\xi=1}^N S_\xi \omega_\xi, \quad (4)$$

where ΔG° , λ_{AD} , ω_ξ , and S_ξ represent the driving force $E_A^\circ - E_D^\circ$, the environmental reorganization energy associated with the charge separation, the frequency, and the Huang-Rhys factor of the ξ th vibrational mode, respectively. The so-called line-broadening function $g_D(t)$ is given as $g_D(t) = \int_0^t ds \int_0^s ds' C(s')/\hbar^2$, where the quantum correlation function $C(t) = \langle X_{AD}(t)X_{AD}(0) \rangle_D$ is expressed with the spectral density $J(\omega)$, namely $C(t) = (\hbar/\pi) \int_0^\infty d\omega J(\omega) [\coth(\beta\hbar\omega/2) \cos \omega t - i \sin \omega t]$. It is noted that Eq. (3) yields the Marcus formula⁴² and the Jortner-Bixon formula⁴³ to describe the condensed phase electron transfer reaction by applying further approximations. To evaluate Eq. (3), the spectral density is decomposed into the environmental and vibrational contributions, $J(\omega) = J_{\text{env}}(\omega) + J_{\text{vib}}(\omega)$. We investigate the timescales of the environmental dynamics affecting the electronic transition energies by modelling the environmental component with the Drude-Lorentz spectral density,⁴⁴ $J_{\text{env}}(\omega) = 2\lambda_{AD}\tau\omega/(\tau^2\omega^2 + 1)$, where τ indicates the time constant of the environmental reorganization dynamics associated with the transition from the

electron donor state to the acceptor state. However, Eq. (3) is not capable of fully describing the environmental dynamics such as the dynamic solvent effect on the charge separation. Hence, we employ the adjusted rate expression,^{45,46}

$$k = \frac{1}{1 + \alpha V_{\text{DA}}^2 \tau} k^{(2)}, \quad (5)$$

where α will be determined by comparing the τ - and V_{DA} -dependence of the rate with the numerically accurate ones, yielding $\alpha = 0.005/\hbar$ in this work. The vibrational component, $J_{\text{vib}}(\omega)$ is modelled with the multimode Brownian oscillator model,⁴⁴ in which the relaxation rate of each mode is given by γ_{ξ} . The applicability of Eq. (5) is verified by comparing the resultant rates with the numerically accurate ones (Fig. 4).

III. RESULTS AND DISCUSSIONS

A. Influence of a specific vibrational mode

We explore the impacts of specific intramolecular vibrations of frequency ω_{vib} and Huang-Rhys factor S_{vib} . Figure 4 presents the rates of the charge separation at the physiological temperature $T = 300$ K as a function of the driving force, $-\Delta G^\circ$, calculated with Eq. (5) (red solid lines) and the numerically accurate quantum dynamics calculations (green filled circles). For the vibrational modes involved in this calculations, we choose two of the intramolecular modes with relatively large Huang-Rhys factors for the transitions of $\text{Chl}^* \rightarrow \text{Chl}^+$ and $\text{Pheo} \rightarrow \text{Pheo}^-$ in Fig. 3, i.e. $\omega_{\text{vib}} = 340 \text{ cm}^{-1}$, $S_{\text{vib}} = 0.035$ (Figs. 4a–4c) and $\omega_{\text{vib}} = 707 \text{ cm}^{-1}$, $S_{\text{vib}} = 0.047$ (Figs. 4d–4f). These two modes may correspond to the modes addressed by Romero *et al.*¹⁵ and Fuller *et al.*¹⁶ As the interstate coupling strength, we assume $V_{\text{DA}} = 70 \text{ cm}^{-1}$, which is the value that is employed in the literature pertaining to the PSII RC.^{23,39} The environmental reorganization time is set to be $\tau = 50$ fs, and the vibrational relaxation rate is $\gamma_{\text{vib}}^{-1} = 2$ ps. For reference purposes, the charge separation rates calculated in the absence of the vibrational contributions are also presented (blue dashed lines and orange open circles). Figures 4a–4c indicate that the 340 cm^{-1} vibrational mode does not play a significant role over a wide range of the reorganization energy and the driving force under the influence of the protein environment. On the other hand, Figs. 4d–4f shows that the 707 cm^{-1} vibrational mode contributes more strongly to the enhancement of the rate, in particular in the vicinity of $-\Delta G^\circ = \omega_{\text{vib}} + \lambda_{\text{AD}}$, where the vibrationally excited state in the acceptor state resonates with the equilibrated donor state. However, an increase in the reorganization energy results in a decrease in the vibrational contribution. The larger amplitude of the fluctuations eradicate the electronic-vibrational resonance, as was discussed in Refs. 25 and 26.

However, it should not be overlooked that the Huang-Rhys factors in the reaction center protein may be several times larger than the values given in Fig. 3, as was discussed before. To further clarify the extent of the vibrational contri-

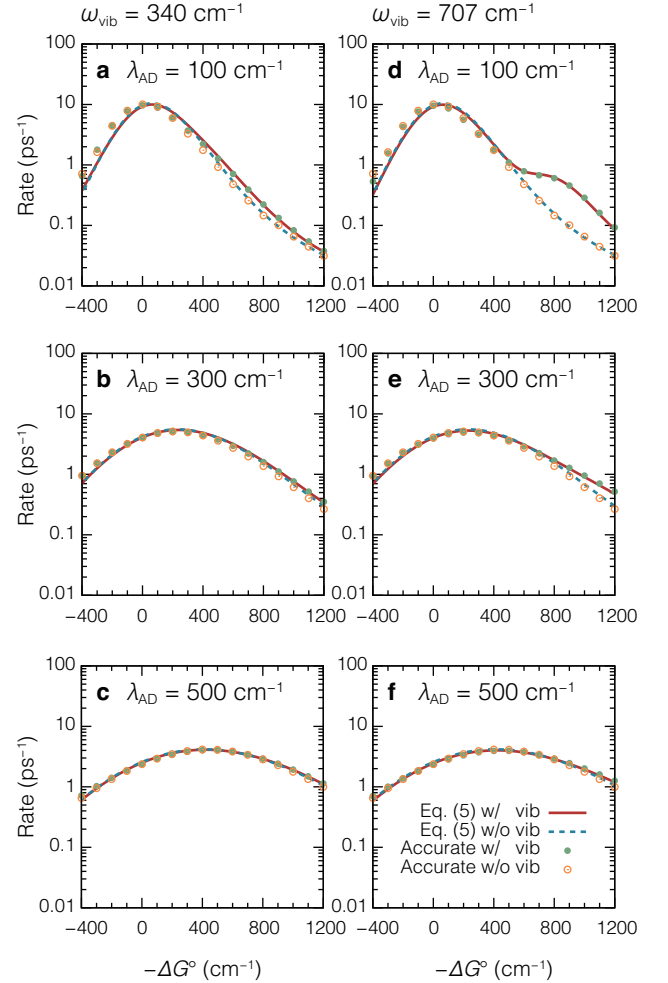


FIG. 4. Rates of the charge separation influenced by specific vibrational modes, 340 cm^{-1} and 707 cm^{-1} . The calculated rates are presented as a function of the driving force $-\Delta G^\circ = E_{\text{D}}^\circ - E_{\text{A}}^\circ$ for various values of the environmental reorganization energy associated with the charge separation, λ_{AD} . Calculations were conducted with Eq. (5) with $\alpha = 0.005/\hbar$ (red solid lines) and the numerically accurate quantum dynamics calculation (green filled circles) including a vibrational mode. For the purpose of comparison, results in the absence of the vibrational mode are also shown (blue dashed lines, orange open circles). The panels on the left (a–c) present the results for the vibrational mode of frequency $\omega_{\text{vib}} = 340 \text{ cm}^{-1}$ and the Huang-Rhys factor $S_{\text{vib}} = 0.035$, whereas those on the right (d–f) for the mode of $\omega_{\text{vib}} = 707 \text{ cm}^{-1}$ and $S_{\text{vib}} = 0.047$. The other parameters are set to be $V_{\text{DA}} = 70 \text{ cm}^{-1}$, $\tau = 50$ fs, $\gamma_{\text{vib}}^{-1} = 2$ ps, and $T = 300$ K.

butions, we examine the dependence of the Huang-Rhys factor on the rate in Fig. 5. The driving force is fixed to be $-\Delta G^\circ = \lambda_{\text{AD}} + \hbar\omega_{\text{vib}}$. Figures 5a–5c show the results for the 340 cm^{-1} mode, and Figs. 5d–5f show those for the 707 cm^{-1} mode in accordance with Fig. 4. When the reorganization energy is small ($\lambda_{\text{AD}} = 100 \text{ cm}^{-1}$), the rate enhancement caused by the larger Huang-Rhys factors is prominent. Nevertheless, when the reorganization energy is assigned values that are physically more reasonable ($\lambda_{\text{AD}} > 300 \text{ cm}^{-1}$), the rate

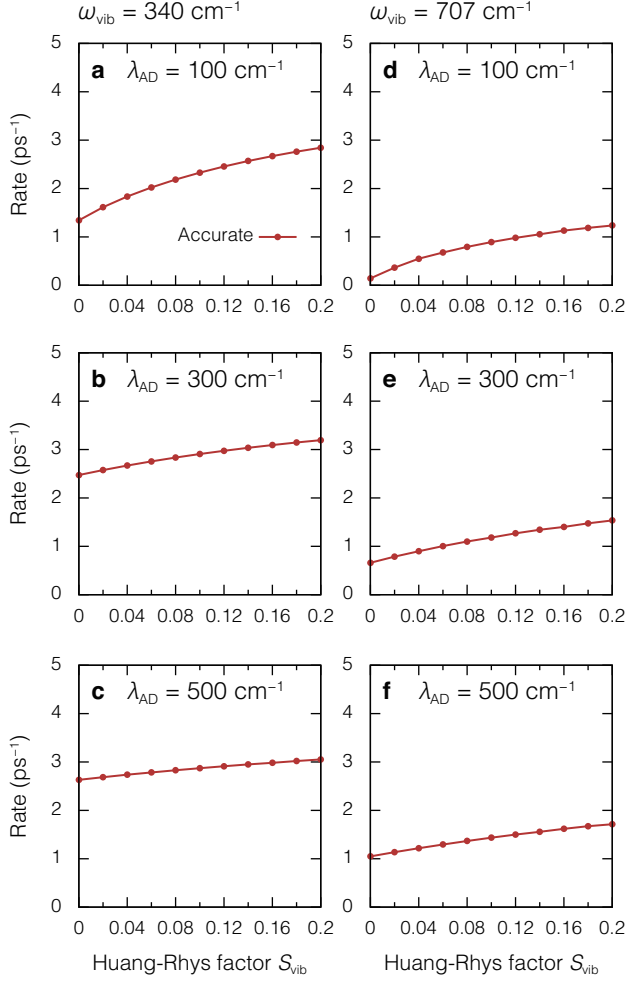


FIG. 5. Huang-Rhys factor dependence of the charge separation rates. The calculated rates are presented as a function of the Huang-Rhys factor S_{vib} for the case of $-\Delta G^\circ = \hbar\omega_{\text{vib}} + \lambda_{\text{AD}}$, where the vibrationally excited state in the acceptor state resonates with the equilibrated donor state. The rates were obtained with the use of the numerically accurate quantum dynamics calculations. The panels on the left (a–c) present the results for the vibrational mode of frequency $\omega_{\text{vib}} = 340 \text{ cm}^{-1}$, whereas those on the right (d–f) contain the results for the mode of $\omega_{\text{vib}} = 707 \text{ cm}^{-1}$. The other parameters are set to be $V_{\text{DA}} = 70 \text{ cm}^{-1}$, $\tau = 50 \text{ fs}$, $\gamma_{\text{vib}}^{-1} = 2 \text{ ps}$, and $T = 300 \text{ K}$.

becomes less sensitive to the Huang-Rhys factors.

To deepen our insight into the charge separation mechanism, the free energy surfaces of the electron donor and acceptor states are investigated with respect to the environmental component \mathcal{E} in the collective energy gap coordinate X_{AD} ,^{36,40,41,47}

$$G_{\text{D}}(\mathcal{E}) = E_{\text{D}}^\circ + \frac{1}{4\lambda_{\text{AD}}} \mathcal{E}^2, \quad (6)$$

$$G_{\text{A}}(\mathcal{E}) = E_{\text{A}}^\circ + \frac{1}{4\lambda_{\text{AD}}} (\mathcal{E} - 2\lambda_{\text{AD}})^2. \quad (7)$$

The intersection between $G_{\text{D}}(\mathcal{E})$ and $G_{\text{A}}(\mathcal{E})$ is located at $\mathcal{E}^* = \Delta G^\circ + \lambda_{\text{AD}}$, yielding the free energy of activation that enables

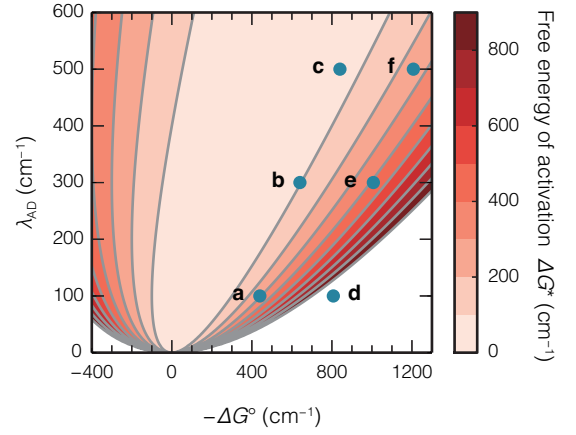


FIG. 6. Contour plot of the free energy of activation required for the charge separation to proceed. The free energy of activation ΔG^* is plotted as a function of the driving force $-\Delta G^\circ = E_{\text{D}}^\circ - E_{\text{A}}^\circ$ and the reorganization energy associated with the charge separation, λ_{AD} . Contour lines are drawn at 100 cm^{-1} intervals. The marked points indicate the sets of $-\Delta G^\circ$ and λ_{AD} that satisfy $-\Delta G^\circ = \hbar\omega_{\text{vib}} + \lambda_{\text{AD}}$ for the vibrational frequencies $\omega_{\text{vib}} = 340 \text{ cm}^{-1}$ (a–c) and $\omega_{\text{vib}} = 707 \text{ cm}^{-1}$ (d–f), corresponding to Figs. 4 and 5. At physiological temperature $T = 300 \text{ K}$, the thermal energy is evaluated as $k_{\text{B}}T \approx 200 \text{ cm}^{-1}$.

the charge separation to proceed as

$$\Delta G^* \approx \frac{(\Delta G^\circ + \lambda_{\text{AD}})^2}{4\lambda_{\text{AD}}}. \quad (8)$$

Figure 6 presents 2D contour plots of ΔG^* as a function of the driving force $-\Delta G^\circ = E_{\text{D}}^\circ - E_{\text{A}}^\circ$ and the environmental reorganization energy λ_{AD} . Contour lines are drawn at 100 cm^{-1} intervals. The plots reveal that the free energy of activation is small in comparison with the thermal energy $k_{\text{B}}T \approx 200 \text{ cm}^{-1}$ at $T = 300 \text{ K}$ across a broad range of the 2D space. In such almost activationless situations, the primary charge separation takes place in a facile fashion without the help of high-frequency vibrational modes, and hence the vibrational modes play a minor role in promoting the charge separation. In the situation satisfying $-\Delta G^\circ = \hbar\omega_{\xi} + \lambda_{\text{AD}}$, the first excited state of the ξ th mode in the acceptor state resonates with the equilibrated donor state, and thus the ξ th mode would be deemed to play a role in promoting the charge separation. In the situation corresponding to Fig. 4a ($-\Delta G^\circ = 440 \text{ cm}^{-1}$, $\omega_{\xi} = 340 \text{ cm}^{-1}$ and $\lambda_{\text{AD}} = 100 \text{ cm}^{-1}$), however, the free energy of activation is evaluated as 289 cm^{-1} , which is comparable to the thermal energy, and hence the 340 cm^{-1} vibrational mode plays a minor role in Fig. 4a. In the situation of Fig. 4d ($-\Delta G^\circ = 807 \text{ cm}^{-1}$, $\omega_{\xi} = 707 \text{ cm}^{-1}$ and $\lambda_{\text{AD}} = 100 \text{ cm}^{-1}$), on the other hand, the free energy of activation is 1249 cm^{-1} , which is much higher than the thermal energy. Therefore, the 707 cm^{-1} mode plays a crucial role in enhancing the charge separation rate in Fig. 4d. The vibrational contributions in Figs. 4b, 4c, 4e, and 4f can be understood in a similar fashion.

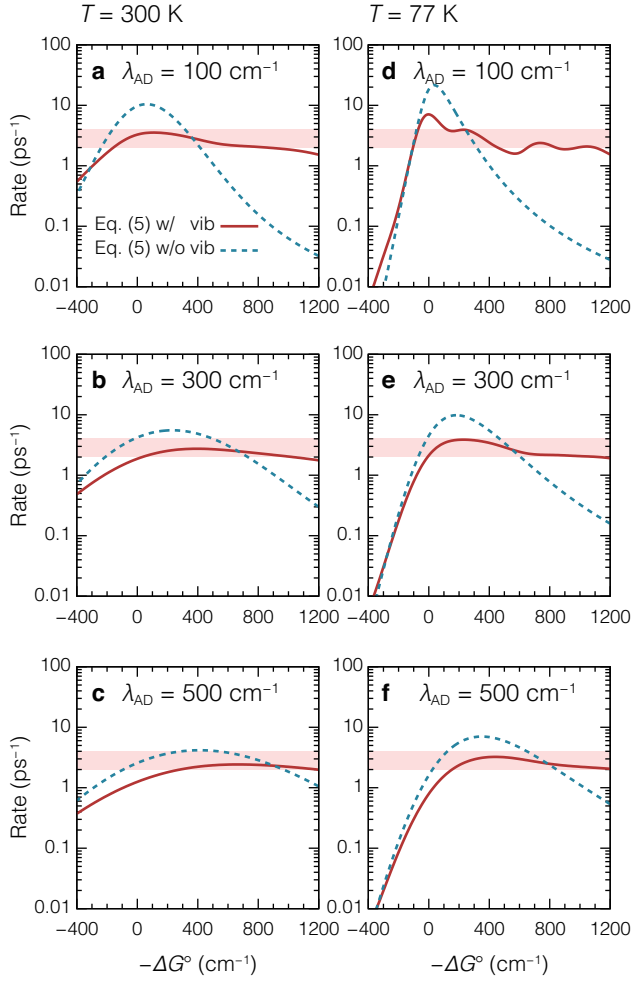


FIG. 7. Rate of the charge separation influenced by all of the vibrational modes in chlorophyll and pheophytin molecules. Calculated rates are presented as a function of the driving force $-\Delta G^\circ$ for various values of the environmental reorganization energy associated with the charge separation, λ_{AD} . Calculations were carried out with Eq. (5) with $\alpha = 0.005/\hbar$ in the presence of all the vibrational contributions (red solid lines) and in the absence of the vibrational contribution (blue dashed lines). The panels on the left (a–c) present the results for the physiological temperature $T = 300$ K, whereas those on the right (d–f) contain the results for the cryogenic temperature $T = 77$ K. The Huang-Rhys factors presented in Fig. 3 are employed to evaluate Eq. (5). The other parameters are set to be $V_{DA} = 70$ cm⁻¹, $\tau = 50$ fs, and $\gamma_\xi^{-1} = 2$ ps.

B. Contribution of all vibrational modes

We investigate the rate of the charge separation influenced by all of the vibrational modes ($\omega_\xi < 1200$ cm⁻¹) in chlorophyll and pheophytin molecules given in Fig. 3. Figure 7 presents the rate as a function of the driving force $-\Delta G^\circ$ for various values of the environmental reorganization energy λ_{AD} . The panels on the left (a–c) present the results for the physiological temperature $T = 300$ K, whereas those on the right (d–f) present those for the cryogenic temperature $T = 77$ K. The calculations were performed with Eq. (5), of which the appli-

cability is verified in Fig. 4. Although the rate enhancement caused by individual vibrational modes is small as in Fig. 4, these small contributions accumulate to make a large difference, in particular in the inverted region, $-\Delta G^\circ > \lambda_{AD}$. On the other hand, the rate is observed to decrease in the normal region, $-\Delta G^\circ < \lambda_{AD}$. An electron transfer reaction occurring in the normal region typically involves only vibrationally ground states, and the coupling between the donor and acceptor states is described with the Franck-Condon factors of the involved vibrational modes as $V_{DA} \rightarrow V_{DA} \prod_{\xi=1}^N e^{-S_\xi/2}$. See Eq. (C2). This reduction in the interstate coupling is responsible for the suppression of the charge transfer rate in the normal region. The vibrational contributions not only cause the rate enhancement in the inverted region but also the rate suppression in the normal region. Consequently, the time constant of the charge separation is maintained to be sub-picosecond, which is consistent with the experimental results,^{8–10} over a wide range of the driving force $-\Delta G^\circ$ and the environmental reorganization energy λ_{AD} . In general, static disorder in systems with larger reorganization energy is stronger, and Gelzinis *et al.* obtained the large static disorder (~ 550 cm⁻¹) by analyzing multiple optical spectra of the PSII RC.²⁴ In this respect, Fig. 7 indicates the inherent robustness of the rate of the primary charge separation in the PSII RC against the disorder in the involved electronic energies as well as in the environmental reorganization energy. Moreover, the insensitivity to temperature variations (77 – 300 K) is consistent with the experimental results of the sub-picosecond transient absorption spectroscopy by Groot *et al.*⁵

IV. CONCLUSION

In conclusion, we determined that the electronic-vibrational resonance of individual vibrational modes plays a minor role in promoting the charge separation processes in the protein environment, contrary to the discussion in recent publications.^{15,16} The free energy of activation required for the charge separation to proceed is no larger than the thermal energy at physiological temperatures over a wide range of the environmental reorganization energy and the driving force. Hence, the charge separation can take place in a facile fashion without the assistance of the high-frequency vibrational modes. However, our examination of the impacts of all of the intramolecular vibrations revealed that these small contributions add up to ultimately have a large influence on the charge separation rate, namely a decrease in the normal region and an increase in the inverted region. This change enables the charge separation rate of sub-picoseconds to be almost independent of the driving force, environmental reorganization energy, and temperature variations. We suggest that intramolecular vibration may represent an important design principle that enables the high quantum efficiency of charge separation in oxygenic photosynthesis in the sense that it complements the robustness of the charge separation in the photosystem II reaction center against the inherently large static disorder of the involved electronic energies.

Appendix A: Quantum chemical calculations

Higashi *et al.*⁴⁸ demonstrated that time-dependent density functional theory (TDDFT) with a range-separated hybrid functional, CAM-B3LYP³⁰ reproduced the lowest singlet excitation energy of bacteriochlorophylla (BChl_a) in various organic solvents. This functional describes the long-range correction to the DFT exchange functional scheme by mixing the DFT short-range term with the Hartree-Fock exchange-integral term that expresses long-range orbital-orbital-exchange interactions, depending on the electronic distance.³⁰ The mixing is characterized by the parameter μ . In the original CAM-B3LYP, the value of μ is set to be 0.33; however, Higashi *et al.* found that the Q_y transition energy of BChl_a in organic solvents was best reproduced by employing $\mu = 0.2$.⁴⁸ With this value, they also succeeded in reproducing the Q_y transition energies of the seven BChl_a molecules embedded in the Fenna-Matthews-Olson protein of green sulfur photosynthetic bacteria.⁴⁹ Along this line, Saito *et al.*⁵⁰ demonstrated that TDDFT calculations with the CAM-B3LYP parameter $\mu = 0.14$ reproduced the observed Q_y transition energies of Chl_a and Chl_b in organic solvents, suggesting $\mu = 0.14$ would be applicable to Chl_a/Chl_b-binding proteins such as PSII and light harvesting complex II (LHCII). In this study, therefore, we perform TDDFT calculations based on the CAM-B3LYP functional with $\mu = 0.14$ for geometry optimization of Chl_a and Pheo_a molecules. We used the 6-31G(d) basis set as in the previous study.⁵⁰ The computational cost was reduced by replacing the long alkyl chains in Chl_a and Pheo_a molecules with methyl groups.⁴⁸

Appendix B: Numerically accurate quantum dynamics calculations

By utilizing the definition of the solvation coordinate X_{AD} , the Hamiltonian in Eq. (1) is recast into the system-plus-environment form,

$$H = H_{\text{sys}} + H_{\text{sys-env}} + H_{\text{env}} \quad (\text{B1})$$

with $H_{\text{sys}} = \varepsilon|D\rangle\langle D| + (\varepsilon + \hbar\Omega_{AD})|A\rangle\langle A| + V_{DA}(|D\rangle\langle A| + |A\rangle\langle D|)$, $H_{\text{sys-env}} = X_{AD}|A\rangle\langle A|$, and $H_{\text{env}} = H_D$. Here, ε is an arbitrary c-number. An adequate description of the charge separation dynamics is provided with the reduced density operator, i.e. the partial trace of the density operator of the total system over the environmental and nuclear DOFs. When the environmentally induced fluctuations are described as Gaussian processes and the relevant nuclear dynamics are

harmonic, the time evolution of the reduced density operator for the Hamiltonian can be integrated in a numerically accurate fashion by using the so-called hierarchical equations of motion approach.⁵¹ The charge separation rate is evaluated in accordance with Ref. 52.

Appendix C: The Marcus and Jortner-Bixon formulae

In Eq. (3), we assume the following: [1] the high-temperature limit for the environmental DOFs, $\coth(\beta\hbar\omega/2) \approx 2/\beta\hbar\omega$, [2] the short-time approximation for the environmental DOFs, $\cos\omega t \approx 1 - \omega^2 t^2/2$ and $\sin\omega t \approx \omega t$, [3] the low-temperature limit for the vibrational DOFs, $\coth(\beta\hbar\omega/2) \approx 1$, and [4] infinitely slow vibrational relaxation and correspondingly the δ -function form for the vibrational spectral density, $J_{\text{vib}}(\omega) = \sum_{\xi=1}^N \pi\hbar S_{\xi}\omega_{\xi}^2 [\delta(\omega - \omega_{\xi}) - \delta(\omega + \omega_{\xi})]$. Under these assumptions, Eq. (3) leads to the multimodal expression of the Jortner-Bixon formula,⁴³

$$k^{(2)} = \sqrt{\frac{\pi}{\hbar^2 \lambda_{AD} k_B T}} \sum_{n_1=0}^{\infty} \cdots \sum_{n_N=0}^{\infty} \kappa(\{n_{\xi}\}) \quad (\text{C1})$$

with

$$\kappa(\{n_{\xi}\}) = V_{DA}^2 \left(\prod_{\xi=1}^N e^{-S_{\xi}} \frac{S_{\xi}^{n_{\xi}}}{n_{\xi}!} \right) e^{-\Delta G^*(\{n_{\xi}\})/k_B T}. \quad (\text{C2})$$

In the above, non-negative integer n_{ξ} stands for a vibrational quantum number of the ξ th high-frequency mode that satisfies $\hbar\omega_{\xi} > k_B T$. The corresponding free energy of activation $\Delta G^*(\{n_{\xi}\})$ is expressed as $\Delta G^*(\{n_{\xi}\}) = (\Delta G^{\circ} + \lambda_{AD} + \hbar \sum_{\xi=1}^N n_{\xi}\omega_{\xi})^2 / 4\lambda_{AD}$. In the absence of the vibrational contributions ($n_{\xi} \rightarrow 0$ and $S_{\xi} \rightarrow 0$), Eq. (C1) yields the Marcus formula.⁴²

ACKNOWLEDGMENTS

The authors are grateful to Professor Jeffrey Reimers for providing the code of his DUSHIN program. Numerical calculations were partly performed at the Research Center for Computational Science, Okazaki Research Facilities, National Institutes of Natural Sciences. This work was supported by JSPS KAKENHI Grant Numbers 16KT0165, 17H02946, 17K05757, and 18H01937 as well as JSPS KAKENHI Grant Numbers 17H06437 in the Innovative Area ‘‘Innovations for Light-Energy Conversion (I⁴LEC)’’ and 18H04657 in the Innovative Area ‘‘Hybrid Catalysis.’’

* ishizaki@ims.ac.jp

¹ Renger, G. & Renger, T. Photosystem II: The machinery of photosynthetic water splitting. *Photosynth. Res.* **98**, 53–80 (2008).

² van Amerongen, H. & Croce, R. Light harvesting in photosystem II. *Photosynth. Res.* **116**, 251–263 (2013).

³ Renger, T. & Schlodder, E. Primary photophysical processes in photosystem II: Bridging the gap between crystal structure and optical spectra. *Chem. Phys. Chem.* **11**, 1141–1153 (2010).

⁴ Durrant, J. R. *et al.*, A multimer model for P680, the primary electron donor of photosystem II. *Proc. Natl. Acad. Sci. USA* **92**, 4798–4802 (1995).

- 5 Groot, M. L. *et al.* Charge separation in the reaction center of photosystem II studied as a function of temperature. *Proc. Natl. Acad. Sci. USA* **94**, 4389–4394 (1997).
- 6 Prokhorenko, V. I. & Holzwarth, A. R. Primary processes and structure of the photosystem II reaction center: A photon echo study. *J. Phys. Chem. B* **104**, 11563–11578 (2000).
- 7 Romero, E., Novoderezhkin, V. I. & van Grondelle, R. Quantum design of photosynthesis for bio-inspired solar-energy conversion. *Nature* **543**, 355–365 (2017).
- 8 Groot, M. L. *et al.* Initial electron donor and acceptor in isolated Photosystem II reaction centers identified with femtosecond mid-IR spectroscopy. *Proc. Natl. Acad. Sci. USA* **102**, 13087–13092 (2005).
- 9 Holzwarth, A. R. *et al.* Kinetics and mechanism of electron transfer in intact photosystem II and in the isolated reaction center: pheophytin is the primary electron acceptor. *Proc. Natl. Acad. Sci. USA* **103**, 6895–6900 (2006).
- 10 Raszewski, G. & Renger, T. Light harvesting in photosystem II core complexes is limited by the transfer to the trap: Can the core complex turn into a photoprotective mode? *J. Am. Chem. Soc.* **130**, 4431–4446 (2008).
- 11 Fleming, G. R., Martin, J. L. & Breton, J. Rates of primary electron transfer in photosynthetic reaction centers and their mechanistic implications. *Nature* **333**, 190–192 (1988).
- 12 Novoderezhkin, V. I., Dekker, J. P. & van Grondelle, R. Mixing of exciton and charge-transfer states in photosystem II reaction centers: Modeling of Stark spectra with modified Redfield theory. *Biophys. J.* **93**, 1293–1311 (2007).
- 13 Wang, H. *et al.* Protein dynamics control the kinetics of initial electron transfer in photosynthesis. *Science* **316**, 747–750 (2007).
- 14 Suga, M. *et al.* Native structure of photosystem II at 1.95 Å resolution viewed by femtosecond X-ray pulses. *Nature* **517**, 99–103 (2015).
- 15 Romero, E. *et al.* Quantum coherence in photosynthesis for efficient solar-energy conversion. *Nat. Phys.* **10**, 677–683 (2014).
- 16 Fuller, F. D. *et al.* Vibronic coherence in oxygenic photosynthesis. *Nat. Chem.* **6**, 706–711 (2014).
- 17 Schlau-Cohen, G. S., Ishizaki, A. & Fleming, G. R. Two-dimensional electronic spectroscopy and photosynthesis: Fundamentals and applications to photosynthetic light-harvesting. *Chem. Phys.* **386**, 1–22 (2011).
- 18 Scholes, G. D. *et al.*, Using coherence to enhance function in chemical and biophysical systems. *Nature* **543**, 647–656 (2017).
- 19 Picorel, R., Chumanov, G., Torrado, E., Cotton, T. M. & Seibert, M. Surface-enhanced resonance Raman scattering spectroscopy of plant photosystem II reaction centers excited on the edge of the Q_y band. *J. Phys. Chem. B* **102**, 2609–2613 (1998).
- 20 Peterman, E. J. G., van Amerongen, H., van Grondelle, R. & Dekker, J. P. The nature of the excited state of the reaction center of photosystem II of green plants: A high-resolution fluorescence spectroscopy study. *Proc. Natl. Acad. Sci. USA* **95**, 6128–6133 (1998).
- 21 Renger, T. Theory of optical spectra involving charge transfer states: Dynamic localization predicts a temperature dependent optical band shift. *Phys. Rev. Lett.* **93**, 188101 (2004).
- 22 Mančal, T., Valkunas, L. & Fleming, G. R. Theory of exciton-charge transfer state coupled systems. *Chem. Phys. Lett.* **432**, 301–305 (2006).
- 23 Gelzinis, A. *et al.* Tight-binding model of the photosystem II reaction center: Application to two-dimensional electronic spectroscopy. *New J. Phys.* **15**, 075013 (2013).
- 24 Gelzinis, A., Abramavicius, D., Ogilvie, J. P. & Valkunas, L. Spectroscopic properties of photosystem II reaction center revisited. *J. Chem. Phys.* **147**, 115102 (2017).
- 25 Ishizaki, A. & Fleming, G. R. Quantum superpositions in photosynthetic light harvesting: Delocalization and entanglement. *New J. Phys.* **12**, 055004 (2010).
- 26 Fujihashi, Y., Fleming, G. R. & Ishizaki, A. Impact of environmentally induced fluctuations on quantum mechanically mixed electronic and vibrational pigment states in photosynthetic energy transfer and 2D electronic spectra. *J. Chem. Phys.* **142**, 212403 (2015).
- 27 Monahan, D. M., Whaley-Mayda, L., Ishizaki, A. & Fleming, G. R. Influence of weak vibrational-electronic couplings on 2D electronic spectra and inter-site coherence in weakly coupled photosynthetic complexes. *J. Chem. Phys.* **143**, 065101 (2015).
- 28 Frisch, M. J. *et al.* *Gaussian 16 Revision B.01* (Gaussian Inc., Wallingford CT, 2016).
- 29 Reimers, J. R. A practical method for the use of curvilinear coordinates in calculations of normal-mode-projected displacements and Duchinsky rotation matrices for large molecules. *J. Chem. Phys.* **115**, 9103–9109 (2001).
- 30 Yanai, T., Tew, D. P. & Handy, N. C. A new hybrid exchange-correlation functional using the Coulomb-attenuating method (CAM-B3LYP). *Chem. Phys. Lett.* **393**, 51–57 (2004).
- 31 Reimers, J. R. *et al.* Assignment of the Q-bands of the chlorophylls: Coherence loss via Q_x - Q_y mixing. *Sci. Rep.* **3**, 1293 (2013).
- 32 Ribeiro, R. F., Marenich, A. V., Cramer, C. J. & Truhlar, D. G. Use of solution-phase vibrational frequencies in continuum models for the free energy of solvation. *J. Phys. Chem. B* **115**, 14556–14562 (2011).
- 33 Gillie, J. K., Small, G. J. & Golbeck, J. H. Nonphotochemical hole burning of the native antenna complex of photosystem I (PSI-200). *J. Phys. Chem.* **93**, 1620–1627 (1989).
- 34 Hughes, J. L., Conlon, B., Wydrzynski, T. & Krausz, E. The assignment of $Q_y(1, 0)$ vibrational structure and Q_x for chlorophyll *a*. *Phys. Procedia* **3**, 1591–1599 (2010).
- 35 Cho, M. & Silbey, R. J. Nonequilibrium photoinduced electron transfer. *J. Chem. Phys.* **103**, 595–606 (1995).
- 36 Ishizaki, A. Interactions between quantum mixing and the environmental dynamics controlling ultrafast photoinduced electron transfer and its temperature dependence. *Chem. Lett.* **42**, 1406–1408 (2013).
- 37 Rätsep, M. & Freiberg, A. Electron-phonon and vibronic couplings in the FMO bacteriochlorophyll *a* antenna complex studied by difference fluorescence line narrowing. *J. Lumin.* **127**, 251–259 (2007).
- 38 Rätsep, M., Cai, Z.-L., Reimers, J. R. & Freiberg, A. Demonstration and interpretation of significant asymmetry in the low-resolution and high-resolution Q_y fluorescence and absorption spectra of bacteriochlorophyll *a*. *J. Chem. Phys.* **134**, 024506 (2011).
- 39 Novoderezhkin, V. I., Romero, E., Dekker, J. P. & van Grondelle, R. Multiple charge-separation pathways in photosystem II: Modeling of transient absorption kinetics. *Chem. Phys. Chem.* **12**, 681–688 (2011).
- 40 Marchi, M., Gehlen, J. N., Chandler, D. & Newton, M. Diabatic surfaces and the pathway for primary electron transfer in a photosynthetic reaction center. *J. Am. Chem. Soc.* **115**, 4178–4190 (1993).
- 41 Gehlen, J. N., Marchi, M. & Chandler, D. Dynamics affecting the primary charge transfer in photosynthesis. *Science* **263**, 499–502 (1994).
- 42 Marcus, R. A. Electron transfer reactions in chemistry. Theory and experiment. *Rev. Mod. Phys.* **65**, 599–610 (1993).

- ⁴³ Jortner, J. & Bixon, M. Intramolecular vibrational excitations accompanying solvent-controlled electron transfer reactions. *J. Chem. Phys.* **88**, 167–170 (1988).
- ⁴⁴ Mukamel, S. *Principles of Nonlinear Optical Spectroscopy* (Oxford Univ. Press, New York, 1995).
- ⁴⁵ Rips, I. & Jortner, J. Dynamic solvent effects on outer-sphere electron transfer. *J. Chem. Phys.* **87**, 2090–2104 (1987).
- ⁴⁶ Sparpaglione, M. & Mukamel, S. Dielectric friction and the transition from adiabatic to nonadiabatic electron transfer. I. Solvation dynamics in Liouville space. *J. Chem. Phys.* **88**, 3263–3280 (1988).
- ⁴⁷ Fujihashi, Y. & Ishizaki, A. Fluctuations in electronic energy affecting singlet fission dynamics and mixing with charge-transfer state: Quantum dynamics study. *J. Phys. Chem. Lett.* **7**, 363–369 (2016).
- ⁴⁸ Higashi, M., Kosugi, T., Hayashi, S. & Saito, S. Theoretical study on excited states of bacteriochlorophyll *a* in solutions with density functional assessment. *J. Phys. Chem. B* **118**, 10906–10918 (2014).
- ⁴⁹ Higashi, M. & Saito, S. Quantitative evaluation of site energies and their fluctuations of pigments in the Fenna-Matthews-Olson complex with an efficient method for generating a potential energy surface. *J. Chem. Theory Comput.* **12**, 4128–4137 (2016).
- ⁵⁰ Saito, K., Suzuki, T. & Ishikita, H. Absorption-energy calculations of chlorophyll *a* and *b* with an explicit solvent model. *J. Photochem. Photobiol. A* **358**, 422–431 (2018).
- ⁵¹ Tanimura, Y. Stochastic Liouville, Langevin, Fokker-Planck, and master equation approaches to quantum dissipative systems. *J. Phys. Soc. Jpn.* **75**, 082001 (2006).
- ⁵² Ishizaki, A. & Fleming, G. R. Unified treatment of quantum coherent and incoherent hopping dynamics in electronic energy transfer. *J. Chem. Phys.* **130**, 234111 (2009).